INTERNATIONAL JOURNAL FOR NUMERICAL METHODS IN FLUIDS, VOL. 12, 585–604 (1991)

DYNAMICAL EIGENFUNCTION DECOMPOSITION OF TURBULENT CHANNEL FLOW

K. S. BALL

Department of Mechanical Engineering, The University of Texas at Austin, Austin, TX 78712, U.S.A.

L. SIROVICH

Center for Fluid Mechanics, Turbulence and Computation, and Division of Applied Mathematics, Brown University, Providence, RI 02912, U.S.A.

AND

L. R. KEEFE

Center for Turbulence Research, NASA–Ames Research Center, Moffett Field, CA 94035, U.S.A.

SUMMARY

The results of an analysis of low-Reynolds-number turbulent channel flow based on the Karhunen–Loève (K–L) expansion are presented. The turbulent flow field is generated by a direct numerical simulation of the Navier–Stokes equations at a Reynolds number $Re_\tau = 80$ (based on the wall shear velocity and channel half-width). The K–L procedure is then applied to determine the eigenvalues and eigenfunctions for this flow. The random coefficients of the K–L expansion are subsequently found by projecting the numerical flow field onto these eigenfunctions. The resulting expansion captures 90% of the turbulent energy with significantly fewer modes than the original trigonometric expansion. The eigenfunctions, which appear either as rolls or shearing motions, possess viscous boundary layers at the walls and are much richer in harmonics than the original basis functions. Chaotic temporal behaviour is observed in all modes and increases for higher-order eigenfunctions. The structure and dynamical behaviour of the eigenmodes are discussed as well as their use in the representation of the turbulent flow.

KEY WORDS Turbulence Channel flow Karhunen–Loève expansion Eigenfunctions Orthogonal decomposition

1. INTRODUCTION

Turbulent channel flow has been the subject of numerous investigations because of its simple geometry and importance in understanding the turbulence mechanisms of wall-bounded shear flows. Recently, direct numerical simulations have made available a detailed knowledge of the entire turbulent velocity field. This has enabled orthogonal decomposition methods, which require complete and sufficiently resolved data, to be applied in the study of turbulent flows. In these methods the turbulent flow field is expanded in terms of the orthogonal eigenfunctions of the spatial velocity correlation tensor. This expansion, which is optimal in that it provides the most rapidly converging orthogonal expansion in the quadratic mean, is a classical result known as the Karhunen–Loève (K–L) expansion. Its use in the study of turbulence is due to Lumley,[1,2] who proposed it as the basis for a rational and quantitative method of identifying coherent structures.

0271–2091/91/060585–20$10.00

Received 6 May 1989
Revised 31 May 1990

The K–L expansion has several important features. It provides a way to extract the underlying structure of a turbulent flow, yielding insights to its behaviour. The K–L expansion can be used to form a low-dimensional dynamical system to study the chaotic dynamics of turbulent flows. The K–L eigenfunctions can also be implemented directly in a numerical scheme, instead of the usual trigonometric basis functions.

Several recent studies have made use of methods based on the K–L expansion. Chambers *et al.*[3] have investigated its application in the solution of Burgers' equation as a model for turbulence, while Sirovich and Rodriguez[4] investigated the Ginzburg–Landau system. The K–L decomposition has also been applied to a wide variety of numerically simulated turbulent flows, including Taylor–Couette flow[5] and Rayleigh–Bénard convection.[6–8] Two studies have been specifically directed towards wall-bounded shear flows. Aubry *et al.*[9] modelled the wall region of a turbulent boundary layer using experimentally determined eigenfunctions to form a low-dimensional dynamical system, while Moin and Moser[10] applied Lumley's methodology to their numerical simulation of turbulent channel flow.

In this paper the structure and dynamical behaviour of the K–L eigenfunctions, which are extracted from a direct numerical simulation of low-Reynolds-number turbulent flow, are studied. In contrast to Moin and Moser (who investigated a considerably higher-Reynolds-number flow with fine spatial resolution), the temporal behaviour of the eigenfunctions is determined directly from the numerical data set (via Galerkin projection) and no assumptions regarding phase (such as the 'shot noise effect') are required.

2. METHODOLOGY

The analytical approach adopted here follows the programme presented by Sirovich[11–13] for the study of turbulence and the dynamics of coherent structures. These ideas follow from Lumley's suggestion of using the eigenfunctions of the two-point velocity correlation tensor to decompose the flow into its relevant modes.[1,2] Details of this approach, as specifically applied to the channel flow problem considered here, are given below, as well as relevant details about the numerical database.

2.1. Numerical procedure and data

The channel flow data analysed in this paper were generated by a direct numerical simulation of the Navier–Stokes equations, performed by L. Keefe at the NASA–Ames Research Center (see Reference 14 for particular details about the numerical scheme employed). The calculations were performed on a $24 \times 33 \times 12$ grid (in x, y, z—the streamwise, wall-normal and spanwise directions). This is somewhat on the coarse side but adequate for present purposes, and is sufficient to resolve the important features of low-Reynolds-number turbulence such as wall layer streaks. The flow statistics (discussed later) are also consistent with other studies of low-Reynolds-number turbulence. The streamwise and spanwise directions are taken to be periodic, with a computational period $L_x = L_z = 1{\cdot}6\pi$ (400 wall units). The channel half-width is $\delta = 1$ (80 wall units).

The flow simulation has a Reynolds number $Re_\tau = 80$ based on the wall shear velocity u_τ and the channel half-width. This corresponds to a Reynolds number based on the centreline velocity and channel half-width of $Re_c \approx 1500$. The database consists of $N = 500$ realizations

$$u_i^{(n)}(x, y, z) = u_i(x, y, z, n\Delta t), \quad n = 1, 2, \ldots, 500, \tag{1}$$

with a viscous time interval between realizations of $\Delta t^+ = 8{\cdot}4(\nu/u_\tau^2)$. The three components of velocity u_i, $i = 1, 2, 3$, will be denoted as $u_i = (u, v, w)$ in the x-, y- and z-directions respectively.

The eigenfunction calculation, to be described in the following subsection, is performed using the fluctuating components of the velocity field (since these are of primary interest). In fully developed turbulent channel flow, only the streamwise velocity has a mean component, which is a function of y. Thus the flow can be decomposed into its mean and fluctuating parts as follows:

$$\begin{aligned} u(x, y, z, t) &= \bar{u}(y) + u'(x, y, z, t), \\ v(x, y, z, t) &= \quad + v'(x, y, z, t), \\ w(x, y, z, t) &= \quad + w'(x, y, z, t), \end{aligned} \tag{2}$$

where $\bar{u}(y)$, the local mean velocity, is determined by averaging each realization over horizontal planes and time, i.e.

$$\bar{u}(y) = \frac{1}{N}\left(\sum_{n=1}^{N} \frac{1}{L_x L_z} \int_0^{L_x} \int_0^{L_z} u^{(n)}(x, y, z)\, \mathrm{d}x\, \mathrm{d}z \right). \tag{3}$$

In this paper, u, v and w (without primes) will be used to denote the fluctuating velocity components and an overbar will refer to averaging over the horizontal plane and time, as in (3). An average over time alone (ensemble average) will be denoted by angle brackets, i.e.

$$\langle u \rangle = \frac{1}{N} \sum_{n=1}^{N} u^{(n)}. \tag{4}$$

The flow is expanded in Fourier series in the homogeneous directions, while Chebyshev polynomials are used in the non-homogeneous vertical direction. Thus the grid is uniformly spaced in x and z, while the Chebyshev collocation points

$$y_i = \cos[(i-1)\pi/32], \quad i = 1, 2, \ldots, 33, \tag{5}$$

are used in the y-direction.

2.2. *Karhunen–Loève expansion*

The two-point correlation tensor or covariance matrix is defined by

$$K_{ij}(\mathbf{x}, \mathbf{x}') = \langle u_i(\mathbf{x}) u_j(\mathbf{x}') \rangle. \tag{6}$$

For turbulent channel flow, with two homogeneous directions, (6) takes the form

$$K_{ij}(\mathbf{x}, \mathbf{x}') = K_{ij}(x - x', y, y', z - z'). \tag{7}$$

This is a consequence of the flow being translationally invariant in the x- and z-directions, i.e. the transformations

$$T_x: \quad u^{(n)} \to u^{(n)}(x + l_1, y, z) \tag{8a}$$

and

$$T_z: \quad u^{(n)} \to u^{(n)}(x, y, z + l_2) \tag{8b}$$

also give admissible flows for any values of l_1 and l_2.

For a kernel of the form (7), the eigenfunctions have the form

$$\phi_i = \psi_i(m, n; y) \exp\left(\frac{2\pi i m x}{L_x} + \frac{2\pi i n z}{L_z} \right), \tag{9}$$

where m is the streamwise wave number and n the spanwise wave number. The determination of ψ_i then follows from

$$\int_{-\delta}^{\delta} dy' \kappa_{ij}(m, n; y, y') \psi_j^*(m, n; y') = \lambda(m, n) \psi_i(m, n; y), \tag{10}$$

where κ_{ij} is the Fourier transform of K_{ij} in the homogeneous directions and the asterisk denotes the complex conjugate. κ_{ij} is calculated from the numerical data set by first taking the discrete Fourier transform of each realization in the horizontal plane,

$$\hat{u}_i^{(n)}(m, n; y) = \sum_x \sum_z u_i^{(n)}(x, y, z) \exp\left(\frac{2\pi i m x}{L_x} + \frac{2\pi i n z}{L_z} \right), \tag{11}$$

and then averaging the correlation over the entire ensemble:

$$\kappa_{ij}(m, n; y, y') = \langle \hat{u}_i(m, n; y) \hat{u}_j^*(m, n; y') \rangle. \tag{12}$$

Thus the kernel κ_{ij} is Hermitian, non-negative and on physical grounds square integrable, so that the existence of a complete set of vector eigenfunctions $\psi_i(m, n)$ given by (10) is assured.

Since the flow field $u_i(x, y, z)$ is real, its Fourier transform is conjugate symmetric, i.e.

$$\hat{u}_i(m, n; y) = \hat{u}_i^*(-m, -n; y). \tag{13}$$

It is easy to see that this property carries through to the kernel κ_{ij} and its eigenfunctions ψ_i.

Using this approach, an eigenfunction calculation is needed for each horizontal wave number pair (m, n). The integral equation (10) is solved numerically using the trapezoidal rule, with the transformation $y' = \cos\theta$ employed to account for the non-uniformly spaced Chebyshev grid points. The trapezoidal weighting function ω is applied in such a manner as to preserve the symmetry of the kernel κ_{ij}, and results in the discrete characteristic value problem

$$\mathbf{K}\Psi = \lambda\Psi, \tag{14}$$

where

$$\mathbf{K} = \omega^{1/2} \kappa \omega^{1/2} \tag{15a}$$

and

$$\Psi = \omega^{1/2} \psi. \tag{15b}$$

Standard numerical eigenvalue–eigenfunction routines are used to solve (14), and then the inverse transform

$$\psi = \omega^{-1/2} \Psi \tag{16}$$

is applied to determine ψ.

In the present problem the dimension of the complex-valued matrix $\mathbf{K}$ is $\dim \mathbf{K} = 99$ (there are three velocity components defined on 33 vertical grid points), so for each wave number pair there are 99 eigenvalues and 99 eigenfunctions. These will be ranked so that $\lambda_1 > \lambda_2 > \ldots > \lambda_{99}$, with the quantum number q used to specify a particular eigenfunction corresponding to λ_q. To completely specify a given eigenfunction thus requires a triplet $\mathbf{k} = (m, n, q)$. The notation $\lambda(m, n, q) = \lambda_{\mathbf{k}} = \lambda_{mn}^q$ will be adopted for the remainder of this paper.

The eigenfunctions $\psi^{(\mathbf{k})}(y) = \psi_{mn}^q(y)$ are complex vector-valued functions of y. It is noted that the phase and magnitude of an eigenfunction are arbitrary, i.e. an eigenfunction multiplied by any complex constant remains an eigenfunction. If the eigenfunctions are normalized to unit length,

$$(\phi^{(\mathbf{k})}, \phi^{(\mathbf{l})}) = \delta_{\mathbf{kl}}, \tag{17}$$

then the eigenvalues have the representation

$$\lambda_{\mathbf{k}} = \langle |\mathbf{u}, \boldsymbol{\phi}^{(\mathbf{k})}|^2 \rangle. \tag{18}$$

This gives the eigenvalue $\lambda_{\mathbf{k}}$ the interpretation of being the average energy of the flow in the direction (in function space) $\boldsymbol{\phi}^{(\mathbf{k})}$. By summing over all directions, the total mean energy of the flow is obtained:

$$E = \sum_{\mathbf{k}} \lambda_{\mathbf{k}}. \tag{19}$$

Once the eigenfunctions have been determined, we may re-represent the flow $\mathbf{u}$ in terms of the set $\{\boldsymbol{\phi}^{(\mathbf{k})}\}$. This will be discussed in Section 2.5.

2.3. Incompressibility and boundary conditions

Since each eigenfunction $\boldsymbol{\phi}$ can be considered to be an admixture of flow realizations,[11] they must satisfy all of the constraints of the problem. In particular, the eigenfunctions must be incompressible,

$$\nabla \cdot \boldsymbol{\phi} = 0, \tag{20}$$

and they must satisfy the no-slip boundary conditions at the top and bottom channel walls.

The boundary conditions simply require that $\boldsymbol{\phi}(y) = 0$ when $y = \pm\delta$. The incompressibility requirement becomes (for each triplet $\mathbf{k} = (m, n, q)$)

$$\frac{\partial \phi_1}{\partial x} + \frac{\partial \phi_2}{\partial y} + \frac{\partial \phi_3}{\partial z} = 0. \tag{21}$$

Recalling the form of $\boldsymbol{\phi}$ in (9), this becomes

$$\mathrm{i}M\psi_1(y) + \mathrm{i}N\psi_3(y) + \frac{\partial}{\partial y}\psi_2(y) = 0, \tag{22}$$

where the notation

$$M = \frac{2\pi m}{L_x}, \qquad N = \frac{2\pi n}{L_z} \tag{23}$$

is adopted for convenience.

Since $\boldsymbol{\phi}$ is in general complex-valued, both the real and imaginary parts of (22) must be zero, or

$$\frac{\partial}{\partial y}\operatorname{Re}(\psi_2(y)) = M \operatorname{Im}(\psi_1(y)) + N \operatorname{Im}(\psi_3(y)), \tag{24a}$$

$$\frac{\partial}{\partial y}\operatorname{Im}(\psi_2(y)) = -M \operatorname{Re}((\psi_1 y)) - N \operatorname{Re}(\psi_3(y)). \tag{24b}$$

It will be shown in the next subsection how the incompressibility requirement affects the structure of the eigenfunctions.

2.4. Symmetry considerations

The full use of the symmetries inherent in a particular problem is essential in this method of analysis. Not only can the use of symmetries reduce the number of calculations required, but the accuracy of the analysis can be greatly improved. The memory and storage requirements are also

reduced significantly, since the symmetries (together with the continuity equation and the real-valued velocity field) impart certain properties on the eigenfunctions themselves. The use of symmetries as applied in the turbulent channel flow problem is discussed in detail by Sirovich.[12] Both continuous (in the form of translational invariances) and discrete symmetry groups are considered. The consequences of the former have already been discussed in Section 2.2. In this subsection the action of the discrete symmetry group is presented.

The geometry being considered is invariant under the dihedral group of transformations, D_2. In particular, the flow is invariant under vertical reflection,

$$R_y: \quad (x, y, z, u, v, w) \rightarrow (x, -y, z, u, -v, w), \tag{25a}$$

spanwise reflection,

$$R_z: \quad (x, y, z, u, v, w) \rightarrow (x, y, -z, u, v, -w), \tag{25b}$$

and rotation about the x-axis,

$$R_y R_z: \quad (x, y, z, u, v, w) \rightarrow (x, -y, -z, u, -v, -w). \tag{25c}$$

Thus, for a given realization, four new flow fields can be produced, extending the size of the ensemble used to complete the correlation tensor.

The extension of the ensemble size through group actions has several consequences. First, it greatly improves the statistics of the eigenfunction calculation at no additional expense. The error associated with representing any arbitrarily selected flow field as a finite sum of eigenfunctions decreases significantly as the size of the ensemble increases. (The number of samples required to insure the accuracy of the eigenfunction calculation is related to the dimension of the problem.)

The second consequence of using symmetries to extend the data set is that those symmetries are forced upon the eigenfunctions. Specifically, the eigenfunctions will be symmetric (or anti-symmetric) about the midplane of the channel, and the modes with spanwise wave number n will be the spanwise reflection of the modes with wave number $-n$, i.e.

$$R_z: \quad (\phi_1^{(\mathbf{k})}, \phi_2^{(\mathbf{k})}, \phi_3^{(\mathbf{k})}), \mathbf{k} = (m, n, q) \rightarrow (\phi_1^{(\mathbf{k})}, \phi_2^{(\mathbf{k})}, -\phi_3^{(\mathbf{k})}), \mathbf{k} = (m, -n, q). \tag{26}$$

Also, it has been noted that because these eigenfunctions are used in the expansion of a real-valued velocity field, they are conjugate symmetric, i.e. modes with a horizontal wave number pair (m, n) are the complex conjugate of the modes $(-m, -n)$. This property, together with the symmetries D_2, gives the additional (and practical) consequence of reducing the combined storage requirements for any given set of eigenfunctions with horizontal wave numbers $(|m|, |n|)$ by a factor of eight. Furthermore, eigenfunction calculations are only necessary for positive values of (m, n), reducing the computational requirements by a factor of four.

2.5. Determination of time-dependent coefficients

As noted in Section 2.2, the flow field $\mathbf{u}$ may be re-represented in terms of the set of eigenfunctions $\{\boldsymbol{\phi}_{mn}^q\}$,

$$\mathbf{u}(x, y, z, t) = \sum_{\mathbf{k}} a_{\mathbf{k}}(t) \boldsymbol{\phi}^{(\mathbf{k})}(x, y, z), \tag{27}$$

with

$$a_{\mathbf{k}}(t) = (\boldsymbol{\phi}^{(\mathbf{k})}(x, y, z), \mathbf{u}(x, y, z, t)). \tag{28}$$

Taking the above inner product, this becomes

$$a_{\mathbf{k}}(t)=\int_{-\delta}^{\delta}\int_{0}^{L_x}\int_{0}^{L_z}\{\boldsymbol{\phi}^{(\mathbf{k})*}(x, y, z)\mathbf{u}(x, y, z, t)\}\,\mathrm{d}z\,\mathrm{d}x\,\mathrm{d}y. \tag{29}$$

Next, the discrete Fourier transform of $\mathbf{u}$ is introduced, together with the factored form of $\boldsymbol{\phi}$ in (9):

$$a_{\mathbf{k}}(t)=\int_{-\delta}^{\delta}\int_{0}^{L_x}\int_{0}^{L_z}\left\{\left[\exp\left(-\mathrm{i}\frac{2\pi mx}{L_x}\right)\exp\left(-\mathrm{i}\frac{2\pi nz}{L_z}\right)\psi^{(\mathbf{k})*}(y)\right]\right.$$
$$\left.\times\left[\sum_{m',n'}\hat{\mathbf{u}}(m', n'; y, t)\exp\left(\mathrm{i}\frac{2\pi m'x}{L_x}\right)\exp\left(\mathrm{i}\frac{2\pi n'z}{L_z}\right)\right]\right\}\mathrm{d}z\,\mathrm{d}x\,\mathrm{d}y, \tag{30}$$

which simplifies to

$$a_{\mathbf{k}}(t)=L_xL_z\int_{-\delta}^{\delta}\psi^{(\mathbf{k})*}(y)\hat{\mathbf{u}}(m, n; y, t)\mathrm{d}y \tag{31}$$

due to the orthogonality of the complex exponential. Thus the determination of the time-dependent coefficients $a_{\mathbf{k}}(t)$ reduces to a single integration in y at each time step.

From equation (18), provided that the eigenfunctions $\boldsymbol{\phi}^{(\mathbf{k})}$ have been normalized, the following result is obtained:

$$\langle|a_{\mathbf{k}}(t)|^2\rangle=\lambda_{\mathbf{k}}. \tag{32}$$

The coefficients $a_{\mathbf{k}}(t)$ are in general complex, with $a_{\mathbf{k}}(t)=a^*_{-\mathbf{k}}(t)$ (owing to the real-valued velocity field from which they are determined). Since these coefficients are determined by projecting directly from the flow field, the magnitudes and phase information are completely recovered. This method of determining the phase is contrasted to other methods, such as the 'shot noise effect' used by Moin and Moser,[10] which do not utilize the complete time-resolved flow to extract phase information directly. The storage and memory demands of a large simulation with high spatial resolution may make the current method impractical. In order to capture the dynamics of the turbulent flow field, the time interval between realizations must be sufficiently small (certainly less than the integral time scale). However, with the relatively coarse resolution of the simulation used here, the flow could be observed at relatively fine time intervals and the phase was recovered without approximation. Symmetries are not used to extend the length of the time series, since the group operations do not provide new dynamical information. Thus, unlike the eigenfunctions, modes in which $m\neq 0$ and $n\neq 0$ require two separate calculations: one for $a_{\mathbf{k}}(t)$ and another for $a_{-\mathbf{k}}(t)$ (the remaining two modes are the conjugates).

3. RESULTS

3.1. Mean properties of flow and flow statistics

The numerical simulation being considered is for low-Reynolds-number turbulent channel flow with $Re_\tau=80$ ($Re_c\approx 1500$). At these low Reynolds numbers the flow is only weakly turbulent, but there have been several experimental studies showing the existence of sustained turbulence for such flows (see e.g. Reference 15). The well-developed logarithmic region of higher-Reynolds-number flows is not observed, but the flow does exhibit a chaotic spatial and temporal behaviour.

The mean velocity profile $\bar{u}(y)$ is shown in Figure 1 (the velocity field has been non-dimensionalized by the wall shear velocity u_τ). A well-developed linear region is clearly observed

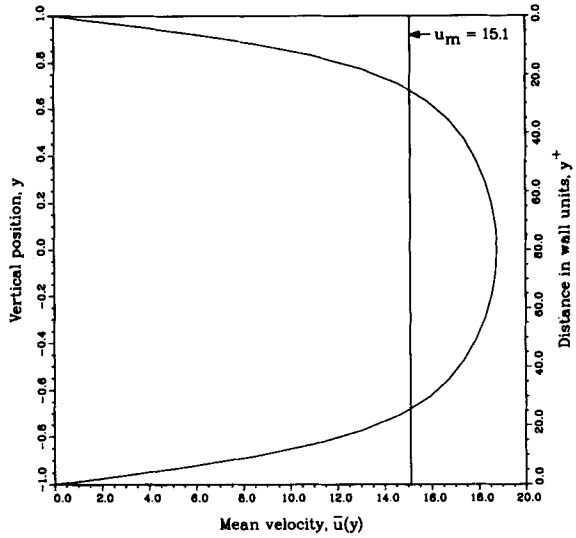

Figure 1. Mean velocity profile $\bar{u}(y)$

close to the wall, although the characteristically blunt profile associated with the logarithmic region of strongly turbulent flows is absent. If the mean velocity $\bar{u}(y)$ is integrated over the channel height 2δ, the bulk mean velocity may be determined:

$$u_m = \frac{1}{2\delta}\int_{-\delta}^{\delta} \bar{u}(y)\,dy. \tag{33}$$

For the flow under consideration, $u_m = 15{\cdot}1$. This is equivalent to the uniform velocity across the channel which gives the same mass flux as the actual non-uniform velocity distribution $\bar{u}(y)$, and is marked on Figure 1 for reference.

If the bulk mean velocity is calculated for each realization, then its variation with time can be shown as in Figure 2. This shows the fluctuations in the mean velocity profile about the time-averaged value $u_m = 15{\cdot}1$. From Figure 2 it is observed that the mass flow rate is initially decreasing, then increases over a long period of time before beginning to decrease again. In other words, the mean velocity profile $\bar{u}(y)$ is undergoing alternate periods of contraction and expansion.

Periods of contraction correspond to periods of increased turbulent activity, with a greater momentum flux from the wall region. Conversely, periods of expansion in the mean velocity profile correspond to decreased levels of turbulence. Evidence for this is provided in Figure 3, where the rate of change in the bulk mean velocity, $(d/dt)u_m(t)$, is compared with the average level of the Reynolds shear stress, $\overline{uv}(t)$. A close correlation is observed between the two curves, as expected.

Finally, the root-mean-square velocity fluctuations across the channel are shown in Figure 4. A fairly strong peak in the streamwise fluctuations occurs near each wall, at $y^+ \approx 15$. This corresponds to the location of the maximum turbulence production, i.e. $-\overline{uv}(\partial\bar{u}/\partial y)$. The spanwise fluctuations show a weaker peak near $y^+ \approx 27$, while the vertical fluctuations are fairly flat throughout the centre of the channel.

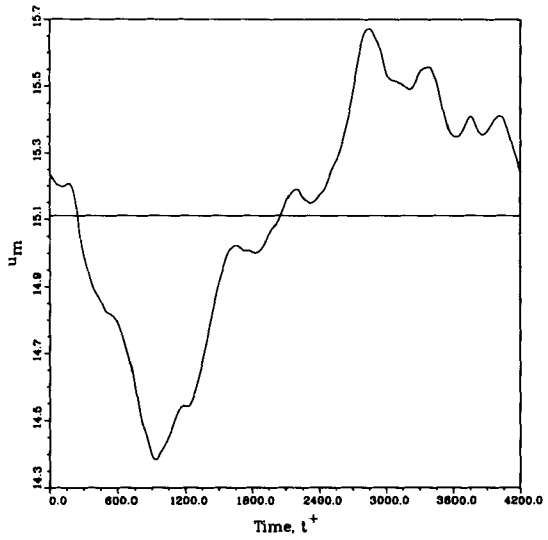

Figure 2. Variations in bulk mean velocity $u_m(t^+)$

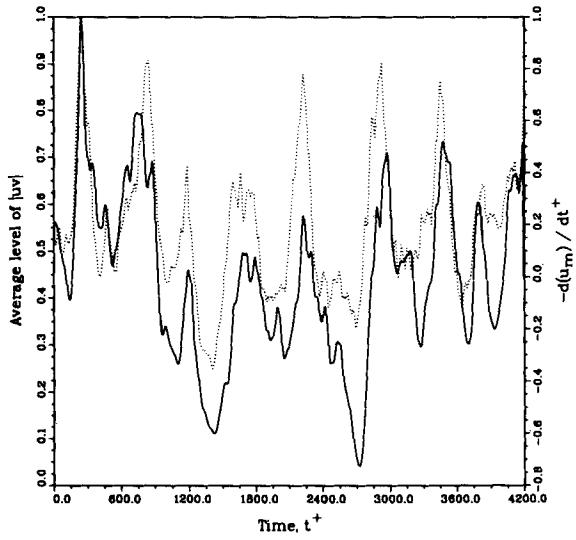

Figure 3. Comparison of the rate of change in the bulk mean velocity with the average level of Reynolds shear stress (variables are scaled by their maximum values): ....., $|uv|$; ——, $-du_m/dt^+$

3.2. Eigenvalue spectrum

As discussed in Section 2.2, the total mean energy in the flow is given by the sum of the eigenvalues (19). Thus each eigenvalue λ_k gives the fraction of the total energy of the eigenfunction associated with it, $\phi^{(k)}$. By ordering the eigenvalues from largest to smallest, the number of eigenfunctions, N, needed to capture a given percentage of the total flow energy in a finite

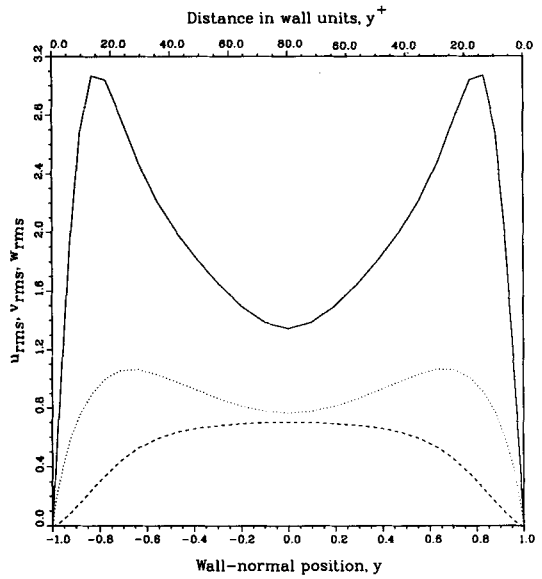

Figure 4. Root-mean-square velocity fluctuations across the channel: ——, u_{rms}; – – –, v_{rms}; . . . . . , w_{rms}

representation of the flow

$$\mathbf{u}(\mathbf{x}, t) = \sum_{\mathbf{k}=1}^{N} a_{\mathbf{k}}(t)\boldsymbol{\phi}^{(\mathbf{k})}(\mathbf{x}), \quad \mathbf{k} = (m, n, q), \tag{34}$$

is minimized. In the above representation, $\mathbf{k}$ is used as an index for the *ordered* eigenfunction $\boldsymbol{\phi}^{(\mathbf{k})}$, with $\lambda_{\mathbf{k}} > \lambda_{\mathbf{k}+1}$.

Table I shows the first 25 eigenfunctions, with the respective energy content and degeneracy for each mode (it is recalled that the symmetries in the problem force certain degeneracies on the eigenfunctions; see Section 2.4). More than half of the energy lies in the first 10 modes (including degeneracies), while over 70% of the energy is captured by the first 25 modes.

In Figure 5 the fraction of energy retained by any finite approximation of the flow is given. One of the properties of the Karhunen–Loève expansion discussed earlier is that it provides the optimal choice of approximating functions in terms of energy content. Thus a finite expansion of the flow field in terms of any other basis would be expected to contain a smaller fraction of energy for the same number of terms. For the Chebyshev–Fourier (C–F) expansion used in the original numerical computations this is indeed the case. The lower curve in Figure 5 corresponds to the C–F expansion and was generated by selecting the Chebyshev and Fourier modes in the order that maximizes the total energy obtainable for a given level of truncation. For approximations with fewer than 50 terms, the K–L eigenfunctions capture nearly twice as much energy as the C–F expansion. In the range $50 \leqslant N \leqslant 1000$ the K–L expansion is still significantly better, but for $N \geqslant 1000$ the advantage decreases, although at a slow rate. This is because the higher-order K–L eigenfunctions become more similar in form to the C–F functions, an indication that there are no significant structures (in terms of energy content) remaining to be resolved in the flow.

The number of K–L eigenfunctions needed to represent the flow accurately (as measured by the energy norm) can be considered as an indication of the *intrinsic dimension* of the space. The usefulness of a K–L dimension d_{KL} as an estimate of attractor dimension is discussed by Sirovich[16] and has been applied in several other studies.[4,7,17] As defined in these studies, d_{KL} is

Table I. Summary of eigenvalue calculation, first 25 values

Index	m	n	q	Eigenvalue	Degeneracy	Energy (fraction of total)
1	0	1	1	0·22671	2	0·1300
2	0	2	1	0·15234	2	0·0874
3	0	3	1	0·12774	2	0·0732
4	0	2	2	0·12077	2	0·0693
5	0	1	2	0·07383	2	0·0423
6	0	3	2	0·07125	2	0·0408
7	1	3	1	0·02857	4	0·0327
8	0	0	1	0·10663	1	0·0305
9	1	3	2	0·02324	4	0·0266
10	0	1	3	0·03279	2	0·0188
11	1	2	1	0·01367	4	0·0156
12	0	0	2	0·05141	1	0·0147
13	1	2	2	0·01195	4	0·0137
14	0	1	4	0·02111	2	0·0121
15	0	2	3	0·02095	2	0·0120
16	1	1	1	0·00932	4	0·0107
17	1	1	2	0·00907	4	0·0104
18	1	2	3	0·00710	4	0·0081
19	0	0	3	0·02783	1	0·0079
20	1	3	3	0·00670	4	0·0076
21	1	3	4	0·00630	4	0·0072
22	2	3	1	0·00620	4	0·0071
23	1	1	3	0·00609	4	0·0069
24	0	3	3	0·01204	2	0·0069
25	0	3	4	0·01173	2	0·0067

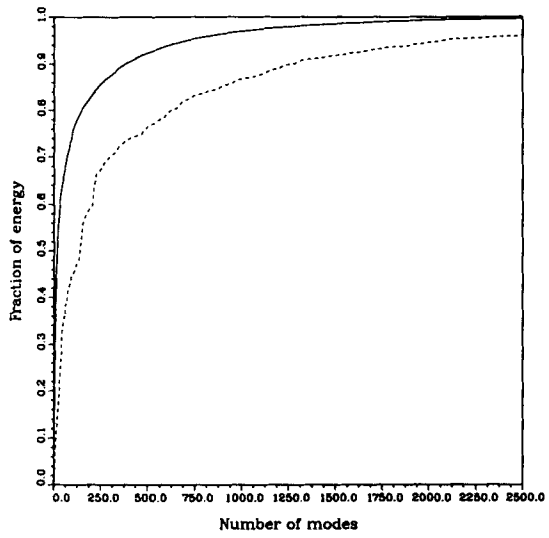

Figure 5. Fraction of energy retained in the Karhunen–Loève expansion (——) compared to the Chebyshev–Fourier expansion (– – –)

the number of eigenfunctions required so that the captured energy is at least 90% of the total and so that no neglected mode, on average, contains more than 1% of the energy contained in the principal eigenfunction mode. In the present case, $d_{KL} = 380$ (degeneracies have been included in the count). It is noted that this *informal* dimension is of the same order as the Lyapunov dimension d_L estimated by Keefe and Moin[18] for this flow using the Kaplan–Yorke procedure, which is $d_L \approx 352$.

3.3. *Structure of eigenfunctions*

In this subsection the spatial structure of three typical eigenfunctions which are representative of the entire set $\{\phi^q_{mn}\}$ is discussed. Recalling that the dependence of the eigenfunctions is factorizable (equation (9)), the vertical structure of each eigenfunction $\psi^q_{mn}(y)$ is presented first, followed by the three-dimensional form of each mode. The spatial structure of the eigenfunctions in the homogeneous horizontal directions is sinusoidal. This results in a roll structure, as in elongated vortices with axes parallel to the horizontal plane. The axis orientation for any given mode is determined by the horizontal wave numbers m and n. As exceptions to this roll structure, some modes appear as shearing motions and will be discussed in further detail later.

In these figures the three components of ψ^q_{mn} corresponding to u, v and w are assembled as real-valued functions. As discussed in Section 2.4, there is a degeneracy associated with each mode due to the symmetries in the problem. By summing over these degeneracies, the real-valued function is obtained (recall that the kernel κ_{ij} in (12) is Hermitian). The eigenfunctions for each mode have been scaled by the maximum absolute value achieved across the channel, maintaining the correct relative scaling between ψ_1, ψ_2 and ψ_3. (The relative scaling between different modes is given by the ratio of their respective eigenvalues and is not shown.).

Some general observations can be made about the eigenfunctions. First, it is readily observed that they satisfy the no-slip boundary conditions at the walls and possess viscous boundary layers. In particular, the vertical gradient of ψ_2, $\partial\psi_2/\partial y$, is zero, as required to satisfy continuity. The eigenfunctions are also symmetric (or antisymmetric) about the midplane. As a consequence, ψ_1 and ψ_2 have opposite parities: when ψ_1 is odd, ψ_2 is even and when ψ_1 is even, ψ_2 is odd. Finally, the eigenfunctions are rich in higher harmonics, with a significant structure in the wall regions. The centre of the channel, by contrast, is relatively flat. The higher-order eigenfunctions are also observed to have generally more zero crossings, which increase in number with the vertical quantum number q.

The first eigenfunction considered has the quantum number triplet $\mathbf{k} = (m, n, q) = (0, 1, 1)$. This is the most energetic mode, i.e. it has the largest eigenvalue. Its vertical structure is shown in Figure 6(a). The streamwise component ψ_1 dominates this mode, with the maximum amplitude of ψ_3 being less than 15% of $\psi_{1,\max}$, while $\psi_{2,\max}$ is approximately 10% of $\psi_{1,\max}$. $\psi_1(y)$ and $\psi_3(y)$ have fairly strong peaks near the wall, at $y^+ \approx 29$ and $y^+ \approx 23$ respectively. The vertical component of the eigenfunction, ψ_2, shows little structure, in contrast to ψ_1 and ψ_3. A vector plot showing the roll structure of this mode in the y–z plane is shown in Figure 6(b). The rolls appear in counter-rotating pairs, and the incompressible nature of the vector field is apparent. All of the modes with $m = 0$ and $n \neq 0$ have forms qualitatively similar to the first eigenfunction of Figure 6.

The next mode, shown in Figure 7, is for $\mathbf{k} = (1, 3, 1)$. This mode also has strong peaks near the walls and is relatively flat in the centre. However, in this mode the maximum value of ψ_3 is nearly 40% of $\psi_{1,\max}$, and $\psi_{2,\max}$ is roughly 20% of $\psi_{1,\max}$. This mode is aligned at an angle $\theta = \tan^{-1}(1/3)$ to the streamwise direction x and carries relatively more energy in the spanwise direction. The roll structure of this mode is shown in the vertical plane normal to the roll axis given by θ.

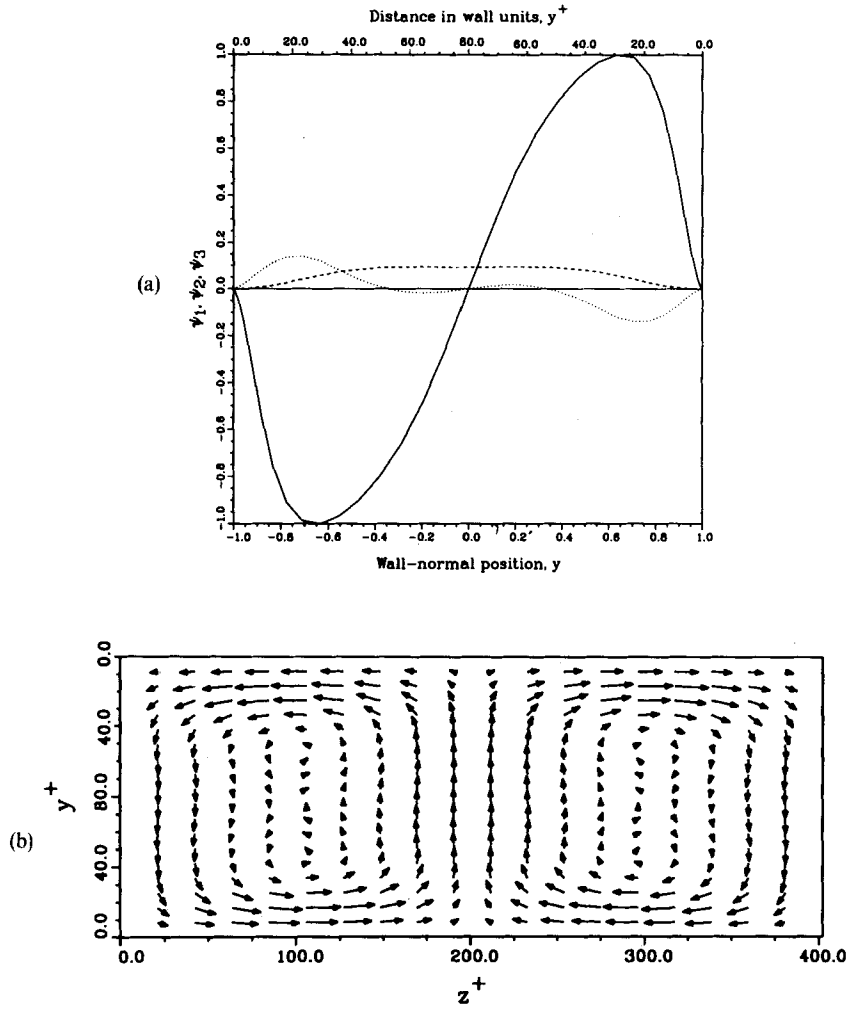

Figure 6. Spatial structure of the eigenfunction with $\mathbf{k}=(0, 1, 1)$: (a) vertical structure $\psi^{(\mathbf{k})}(y)$ (——, ψ_1; – – –, ψ_2; . . . . . , ψ_3); (b) plane cross-section normal to roll axis

Finally, the mode $\mathbf{k}=(0, 0, 1)$, shown in Figure 8, is observed to have only a streamwise component ψ_1. This mode carries information about the mean flow. Since the only mean component in the flow is in the streamwise direction (equation (2)), $\psi_2=\psi_3=0$. The profile of ψ_1 has a relative maximum at roughly $y^+ \approx 9$ and a zero crossing near $y^+ \approx 16$. It is relatively flat in the centre of the channel. Thus this mode has the primary effects of modifying the mean velocity gradient $\partial\bar{u}/\partial y$ in the wall region of the flow, with an accompanying contraction or expansion in the mean velocity profile. Thus the modes with $m=n=0$ are observed to be the mechanism for the temporal variations in u_m discussed in Section 3.1. In Figure 8(b) this mode is observed to be one of the *shearing* modes mentioned earlier. The other notable exception to the roll structure occurs in some modes with $n=0$ (and $m\neq 0$). These modes have an orientation that is perpendicular to the direction of mean flow, i.e. they are aligned in the spanwise direction z. Hence they can only extract energy from the mean flow and are termed *parasitic*.

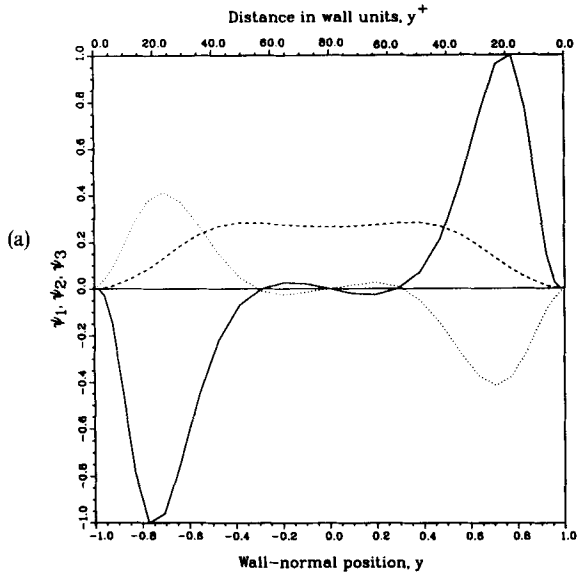

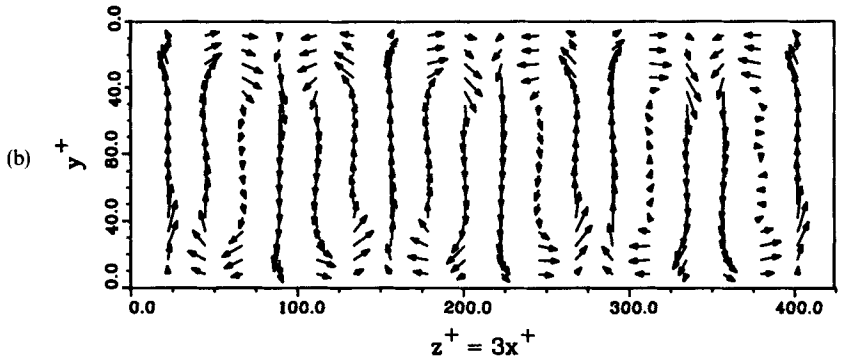

Figure 7. Spatial structure of the eigenfunction with $\mathbf{k}=(1, 3, 1)$: (a) vertical structure, $\psi^{(\mathbf{k})}(y)$ (——, ψ_1; – – –, ψ_2; . . . . . , ψ_3); (b) plane cross-section normal to roll axis

The predominant roll structure of the most energetic eigenfunctions is an important result. It gives the interpretation of elongated vortices to those modes possessing rolls, which provides a mechanism for the transport of fluid away from (or towards) the channel walls. Such a mechanism must be present in order to allow for turbulent 'bursts' or 'sweeps'. Furthermore, the momentum exchange associated with streamwise vortices are responsible for the existence of high- and low-speed streak regions in the boundary layers. The role of the shearing modes is not completely understood, but these modes may be related to the instabilities in the flow, providing a mechanism for the exchange of energy within the flow.

3.4. Modal reconstruction of flow

In Section 2.5 the reconstruction of the instantaneous flow field $\mathbf{u}(\mathbf{x}, t)$ by a finite expansion using the K–L eigenfunctions was discussed. The optimal nature of the K–L expansion in terms of

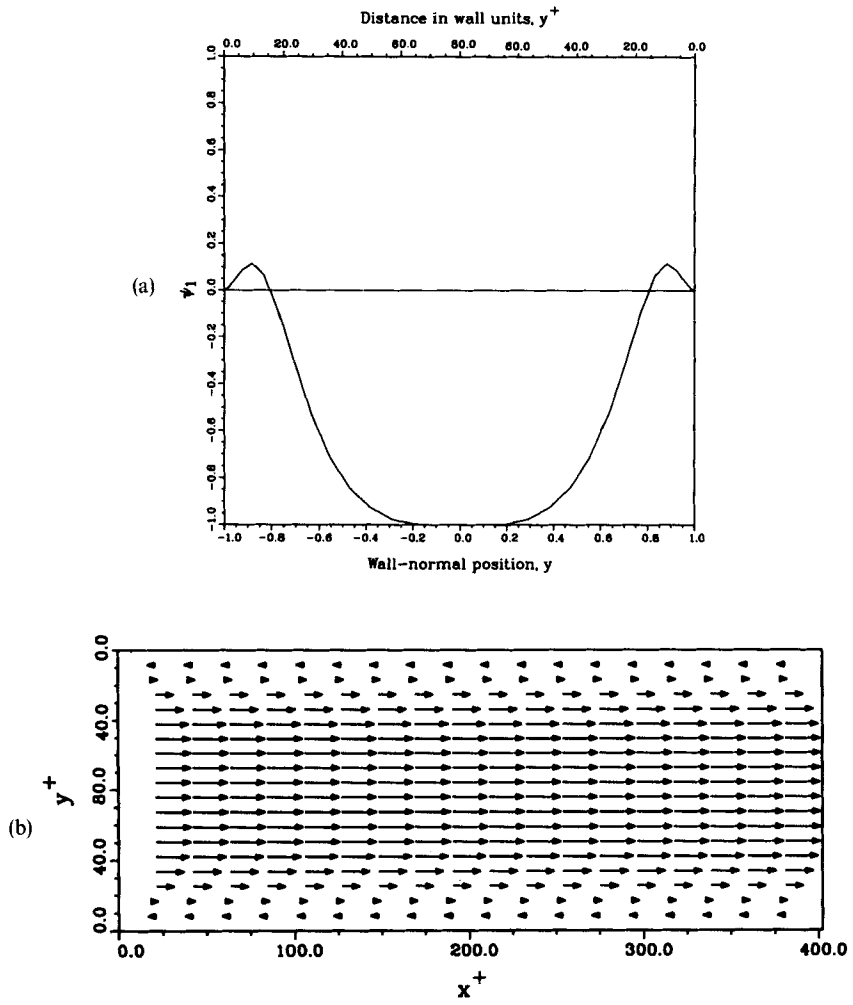

Figure 8. Spatial structure of the eigenfunction with $\mathbf{k}=(0, 0, 1)$: (a) vertical structure, $\psi^{(\mathbf{k})}(y)$; (b) plane cross-section in direction of shear

the percentage of the total energy captured has been demonstrated. By introducing (27) into the definition of the correlation (6) and recalling that the modes are uncorrelated, the following result is obtained:

$$\langle u_i(\mathbf{x})u_j(\mathbf{x})\rangle = \sum_{\mathbf{k}} \lambda_{\mathbf{k}} \phi_i^{(\mathbf{k})}(\mathbf{x})\phi_j^{(\mathbf{k})*}(\mathbf{x}). \tag{35}$$

Thus the contribution of each eigenfunction to the turbulent kinetic energy and Reynolds shear stress can be determined. In this subsection the effectiveness of using the K–L expansion to reproduce the second-order statistics of the flow field is presented.

In Figures 9–11 the convergence of the K–L expansion for the root-mean-square velocity fluctuations across the channel are shown as the number of terms N in the expansion is increased. In all three cases the eigenfunction expansion provides a better approximation to the actual

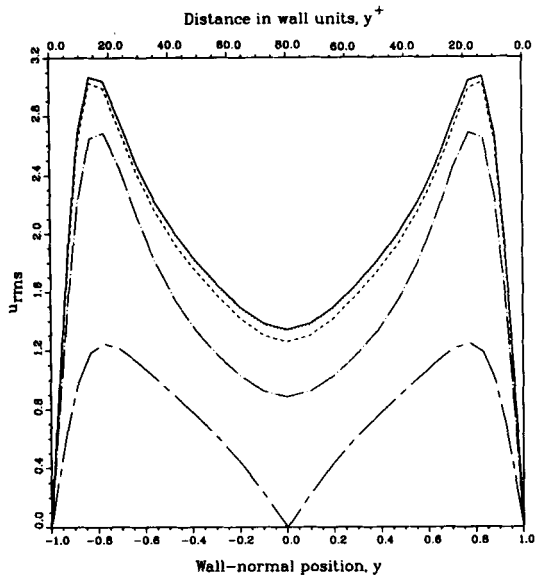

Figure 9. Convergence of the Karhunen–Loève expansion for the root-mean-square streamwise velocity fluctuations: ———, $N=1$; —·—, $N=10$; – – –, $N=100$; ....., $N=500$; ——, exact

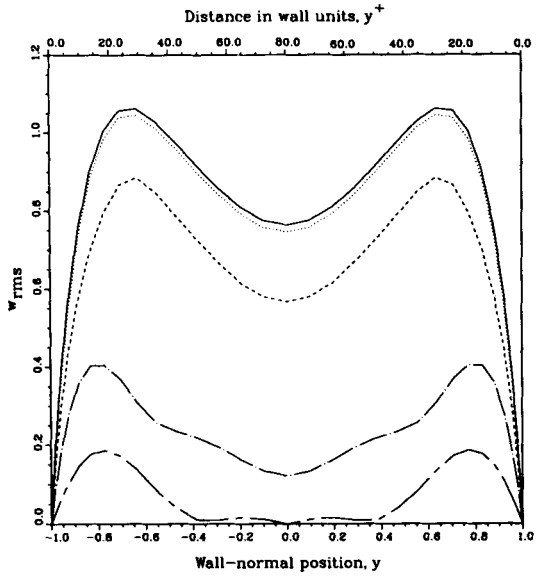

Figure 10. Convergence of the Karhunen–Loève expansion for the root-mean-square spanwise velocity fluctuations: ———, $N=1$; —·—, $N=10$; – – –, $N=100$; ....., $N=500$; ——, exact

profile nearer to the walls than to the centre of the channel. This is particularly evident for the lower-order approximations. The actual profile is also observed to be approached entirely from below, i.e. the higher-order terms all make positive contributions to the energy.

In Figure 12 the convergence of the Reynolds shear stress is shown. As before, the K–L expansion provides a better approximation in the wall region with the lower-order terms.

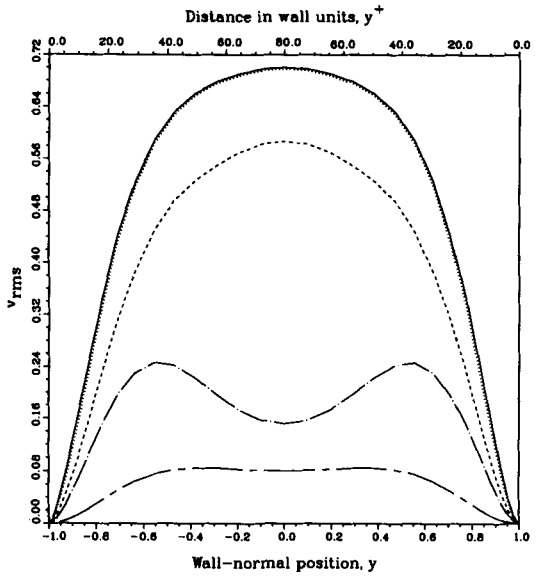

Figure 11. Convergence of the Karhunen–Loève expansion for the root-mean-square wall-normal velocity fluctuations: — — —, $N=1$; — · —, $N=10$; – – –, $N=100$; . . . . . , $N=500$; ——, exact

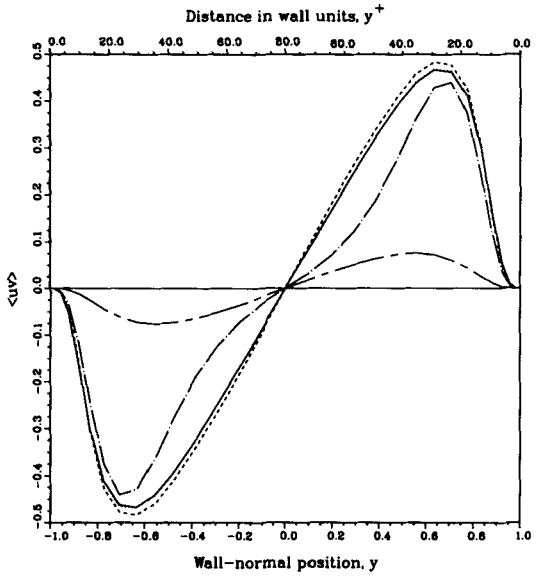

Figure 12. Convergence of the Karhunen–Loève expansion for the mean Reynolds shear stress: — — —, $N=1$; — · —, $N=10$; – – –, $N=100$; . . . . . , $N=500$; ——, exact

However, the approximation with $N=500$ terms is observed to be nearly identical to the actual profile. Furthermore, the approximation with $N=100$ terms shows a greater level of stress at every vertical location. Thus there are negative contributions to the Reynolds shear stress as well as positive contributions at higher orders.

3.5. *Time series and dynamics*

The time course of the power for the three modes discussed in Section 3.3, $|a_{\mathbf{k}}(t)|^2$, is shown in Figures 13–15. The time-dependent coefficients $a_{\mathbf{k}}(t)$ were obtained by projecting the velocity field $\mathbf{u}(\mathbf{x}, t)$ onto the eigenfunctions as outlined in Section 2.5. The mean power for each mode, given by (32), is also shown. The modes display varying degrees of chaos, which seems to increase in the higher-order modes. Fairly large excursions from the mean are also to be noted.

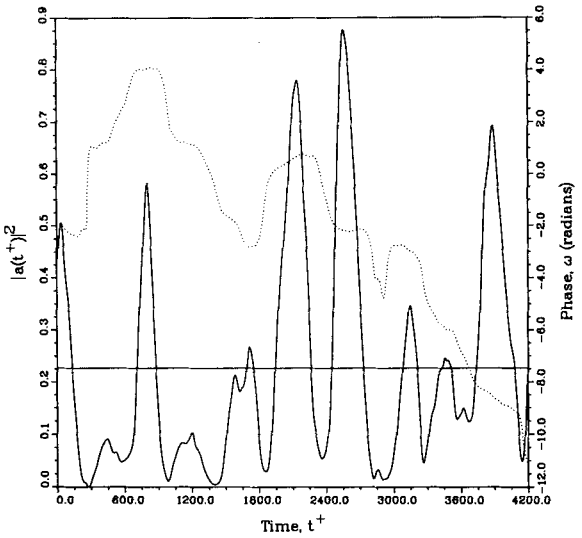

Figure 13. Time series for the eigenfunction with $\mathbf{k}=(0, 1, 1)$: the horizontal line is the eigenvalue for this mode; ——, $|a(t^+)|^2$; ....., ω

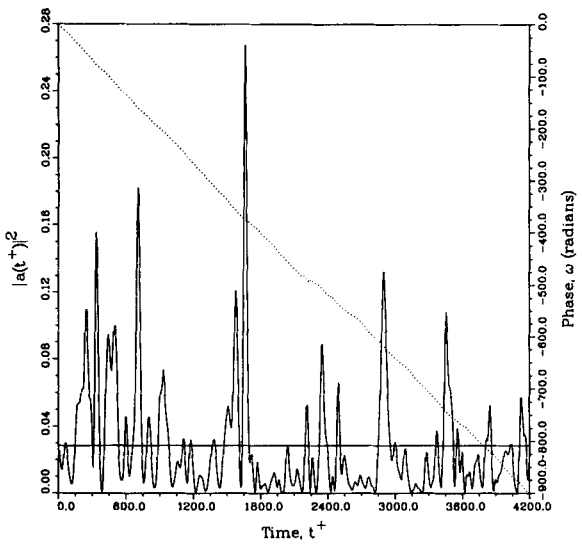

Figure 14. Time series for the eigenfunction with $\mathbf{k}=(1, 3, 1)$: the horizontal line is the eigenvalue for this mode; ——, $|a(t^+)|^2$; ....., ω

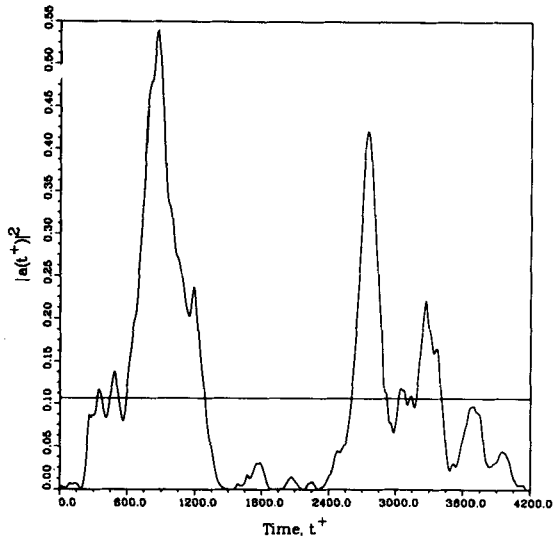

Figure 15. Time series for the eigenfunction with $\mathbf{k}=(0, 0, 1)$: the horizontal line is the eigenvalue for this mode

Also shown in Figures 13 and 14 is the time variation in phase for each mode (note that the (0, 0, 1) mode of Figure 15 is a real function—see Section 2.4—and has no phase). As noted in Section 2.5, the phase information is recovered completely by the projection of equation (28). In the figures the phase (shown in radians) is displayed as a smoothly varying function of time and is not constrained to the interval $[-\pi, \pi]$.

For the modes with $m=0$, such as in Figure 13, qualitatively similar results are obtained. The amplitude variation appears to be dominated by lower frequencies, with higher-frequency motions superimposed. As the mode order increases, the higher frequencies become more visible. The phase, in contrast with the amplitude, meanders in a single direction for much longer periods of time, with higher-frequency variations carried along.

The modes with $m\neq 0$ and $n\neq 0$, such as in Figure 14, show a higher degree of complexity in the amplitude than the other modes. This is perhaps a reflection of the influence of the smaller scales of motion present in these modes. The phase is also observed to be dramatically different in these modes, having a nearly constant rate of change with time throughout the entire plot. This is suggestive of an oblique wave travelling with a characteristic speed through the channel, which may play an important role in the local production of turbulence. This issue is fully discussed in another paper.[19]

The significance of the mode $\mathbf{k}=(0, 0, 1)$ has already been discussed in other sections of this paper. It is associated with time variations in the mean velocity $\bar{u}(y)$. It is interesting to note that its amplitude variation is very closely related to the variation of $u_m(t)$ shown in Figure 2.

4. CONCLUSIONS

The use of the Karhunen–Loève expansion in the analysis of turbulent channel flows has been presented. The methodology followed in this study has been described in detail, providing a complete prescription for the determination of the K–L eigenfunctions and their corresponding

time-dependent coefficients. Particular emphasis has been placed on making full use of the symmetries inherent in the problem.

The results presented show the structure of the eigenfunctions for a low-Reynolds-number turbulent channel flow. The accuracy associated with using the K–L expansion to represent the flow field is demonstrated in terms of the percentage of total energy captured and the ability to approximate the second-order statistics of the flow. Finally, the dynamical behaviour of the eigenfunctions is discussed.

The eigenfunctions together with their time-dependent coefficients have provided the framework for further analysis of this flow. Current investigations into the role of travelling plane waves and shearing motions associated with certain modes are under way. Also, similarities between the K–L eigenfunctions and the Orr–Sommerfeld eigenfunctions are being studied. Finally, a parametric study of the Reynolds number dependence of the K–L eigenfunctions is being conducted, in part to evaluate their potential when used as basis functions in spectral simulations. These results will be reported in later papers.

ACKNOWLEDGEMENTS

The authors gratefully acknowledge support provided by DARPA-URI under contract number N00014-86-K0754. The use of the Pittsburgh Supercomputing Center is also acknowledged.

REFERENCES

1. J. L. Lumley, 'The structure of inhomogeneous turbulent flows', in A. M. Yaglom and V. I. Tatarski (eds), *Atmospheric Turbulence and Radio Wave Propagation*, Nauka, Moscow, 1967, pp. 166–178.
2. J. L. Lumley, *Stochastic Tools in Turbulence*, Academic Press, New York, 1970.
3. D. H. Chambers, R. J. Adrian, P. Moin, D. S. Stewart and H. J. Sung, 'Karhunen–Loève expansion of Burgers' model of turbulence', *Phys. Fluids*, **31**, 2573–2582 (1988).
4. L. Sirovich and J. D. Rodriguez, 'Coherent structures and chaos: a model problem', *Phys. Lett. A*, **120**, 211–214 (1987).
5. A. V. Tangborn, L. Sirovich and C. L. Streett, 'An orthogonal decomposition of finite length chaotic Taylor–Couette flow', *Bull. Am. Phys. Soc.*, **33**, 2242 (1988).
6. L. Sirovich, M. Maxey and H. Tarman, 'Analysis of turbulent thermal convection', *Sixth Symp. on Turbulent Shear Flow*, Toulouse, 1987, in J.-C. André, J. Cousteix, F. Durst, B. E. Launder, F. W. Schmidt and J. H. Whitelaw (eds), *Turbulent Shear Flows 6: Selected Papers from the Sixth International Symposium on Turbulent Shear Flows*, Springer-Verlag, New York, 1987, pp. 68–77.
7. H. Tarman, 'Analysis of turbulent thermal convection', *Ph.D. Thesis*, Brown University, Providence, RI, 1989.
8. T. Howes, L. Sirovich and T. A. Zang, 'Eigenfunction analysis of Rayleigh–Bénard convection', *Bull. Am. Phys. Soc.*, **33**, 2261 (1988).
9. N. Aubry, P. Holmes, J. L. Lumley and E. Stone, 'The dynamics of coherent structures in the wall region of a turbulent boundary layer', *J. Fluid Mech.*, **192**, 115–175 (1988).
10. P. Moin and R. D. Moser, 'Characteristic-eddy decomposition of turbulence in a channel', *J. Fluid Mech.*, **200**, 471–509 (1989).
11. L. Sirovich, 'Turbulence and the dynamics of coherent structures, Pt. I: Coherent structures', *Q. Appl. Math.*, **XLV**, 561–571 (1987).
12. L. Sirovich, 'Turbulence and the dynamics of coherent structures, Pt. II: Symmetries and transformations', *Q. Appl. Math.*, **XLV**, 573–582 (1987).
13. L. Sirovich, 'Turbulence and the dynamics of coherent structures, Pt. III: Dynamics and scaling', *Q. Appl. Math.*, **XLV**, 583–590 (1987).
14. J. Kim, P. Moin and R. Moser, 'Turbulence statistics in fully developed channel flow at low Reynolds number', *J. Fluid Mech.*, **177**, 133–166 (1987).
15. V. C. Patel and M. R. Head, 'Some observations on skin friction and velocity profiles in fully developed pipe and channel flows', *J. Fluid Mech.*, **38**, 181–201 (1969).
16. L. Sirovich, 'Chaotic dynamics of coherent structures', *Physica D*, **37**, 126–145 (1989).
17. L. Sirovich and A. Deane, 'A computational study of Rayleigh–Bénard convection. Part II: Dimension considerations', *J. Fluid Mech.*, in the press.
18. L. R. Keefe and P. Moin, 'The dimension of an attractor in turbulent Poiseuille flow', *Bull. Am. Phys. Soc.*, **32**, 2026 (1987).
19. L. Sirovich, K. S. Ball and L. R. Keefe, 'Plane waves and structures in turbulent channel flow', *Phys. Fluids A*, in the press.